Magnesium implants with alternating magnetic field-enhanced hydrogen release and proton depletion for anti-infection treatment and tissue repair

Nailin Yang [a,b,1], Xiaoyuan Yang [b,1], Shuning Cheng [b,1], Xiang Gao [c], Shumin Sun [b], Xuan Huang [b], Jun Ge [d], Zhihui Han [b], Cheng Huang [c], Yuanjie Wang [b], Chong Cheng [e], Liang Cheng [a,b,*]

[a] Macao Institute of Materials Science and Engineering, Macau University of Science and Technology, Taipa, 999078, Macau SAR, China
[b] Institute of Functional Nano & Soft Materials (FUNSOM), Jiangsu Key Laboratory for Carbon-Based Functional Materials and Devices, Soochow University, Suzhou, 215123, China
[c] Department of Orthopedics, The Second Affiliated Hospital of Soochow University, Suzhou, 215004, China
[d] Department of Orthopedics, The First Affiliated Hospital of Soochow University, Suzhou, 215006, China
[e] College of Polymer Science and Engineering, State Key Laboratory of Polymer Materials Engineering, Sichuan University, Chengdu, 610065, China

ARTICLE INFO

ABSTRACT

Implant-related osteomyelitis is a formidable hurdle in the clinical setting and is characterized by inflammation, infection, and consequential bone destruction. Therefore, effective reactive oxygen species (ROS) scavenging, bacterial killing, and subsequent bone tissue repair are urgently needed for the treatment of difficult-to-heal osteomyelitis. Herein, we utilized the eddy-thermal effect of magnesium (Mg) implants under an alternating magnetic field (AMF) for the controlled release of H_2 gas and ions (OH^- and Mg^{2+}) for the treatment of osteomyelitis. H_2 released by Mg rods under AMFs effectively scavenged cytotoxic ROS, exhibiting anti-inflammatory effects and consequently disrupting the environment of bacterial infections. In addition, the OH^- hindered the energy metabolism of bacteria by effectively neutralizing protons within the microenvironment. Moreover, H_2 impaired the permeability of bacterial membranes and expedited the damage induced by OH^-. This synergistic AMF-induced H_2 and proton depletion treatment approach not only killed both gram-negative and gram-positive bacteria but also effectively treated bacterial infections (abscesses and osteomyelitis). Moreover, Mg^{2+} released from the Mg rods enhanced and accelerated the process of bone osteogenesis. Overall, our work cleverly exploited the eddy-thermal effect and chemical activity of Mg implants under AMFs, aiming to eliminate the inflammatory environment and combat bacterial infections by the simultaneous release of H_2, OH^-, and Mg^{2+}, thereby facilitating tissue regeneration. This therapeutic strategy achieved multiple benefits in one, thus presenting a promising avenue for clinical application.

1. Introduction

The escalating increase in infections, particularly deep tissue infections induced by pathogenic strains, has emerged as a worldwide predicament in human health [1–3]. Deep tissue infection, such as implant-associated osteomyelitis, presents a major challenge in the clinical setting and is characterized by infection and bone destruction, accompanied by chronic inflammation and recurrent bouts of infection [4–6]. At present, the conventional approaches for treating tissue infection involve surgical debridement and the administration of antimicrobial agents. Unfortunately, irregular surgical interventions and inappropriate antibiotic usage have contributed to the emergence of bacterial infections that are resistant to antibiotics and have even given rise to superbugs [7]. Recent research revealed that the surgical procedure itself triggered a profound host response characterized by acute inflammation and cell death resulting from the expression of high levels of reactive oxygen species (ROS) [8]. The excessive accumulation of ROS in tissue not only triggers robust inflammatory reactions, rendering the

tissue susceptible but also hampers the activities of intrinsic stem cells and macrophages, stimulating osteoclasts and bone damage [9]. In addition, elevated levels of ROS often induce local irreversible oxidative damage, leading to heightened inflammation and increased vulnerability to bacterial infections [10]. Therefore, it is crucial to implement efficacious strategies for ROS scavenging, bacterial killing, and subsequent bone tissue repair to treat difficult-to-heal osteomyelitis.

Gas therapy, a burgeoning therapeutic modality, has garnered increasing interest for its application in the treatment of inflammation-related diseases [11–15]. In particular, hydrogen (H_2), as a kind of endogenous gas, can modulate various vital physiological and pathological processes, rendering it efficacious in the treatment of inflammation-related diseases (such as tumors, inflammation, and infections) [16–19]. H_2, which has robust antioxidant properties, can effectively neutralize cytotoxic ROS, such as hydroxyl radicals (•OH), that are highly expressed in inflammatory tissues. Interestingly, H_2 also showed a facilitative impact in bolstering the effectiveness of anti-infective applications [20,21]. However, due to its poor aqueous solubility, the concentration of H_2 enriched in the diseased tissue through traditional drug delivery routes, such as H_2-water or H_2-gas, is often below the necessary level for effectively eliminating locally accumulated ROS. Recently, novel H_2 donors and delivery systems that are responsive to light or ultrasound have been developed [22–24]. For example, novel H_2 donors (e.g., CaH_2, Mg galvanic cells), light-responsive nanomaterials (e.g., $PdH_{0.2}$, TiO_2), and ultrasound-responsive nanomaterials (e.g., $Pt–Bi_2S_3$, C_3N_4) have been developed [16,25–29]. Although ultrasound has a greater penetration depth than laser, the controlled release of H_2 in deep tissues, such as bone tissue, still remains challenging. Thus, it is urgent to develop novel strategies to achieve the on-demand release of H_2 gas in deep tissues.

Alternating magnetic field (AMF), which is not limited by tissue penetration depth, has garnered widespread attention as a local treatment tool recently, such as magnetic hyperthermia therapy (MHT) [30–33]. With the development of novel biomaterials and bio-technologies, the eddy-thermal effect generated by Faraday's law of electromagnetic induction allows macroscopic conductors with low resistivity and high conductivity, exemplified by magnesium (Mg) implants, to generate induced current heating under AMFs [34,35]. Based on the eddy-current effect, several research groups, including our group, have carried out a series of research works on MHT of tumors using macroscopic metals, including Mg implants [36,37]. It is exciting that Mg, as a relatively reactive metal, can produce H_2 gas in a physiological environment, and its eddy-thermal effect under AMFs can be used to heighten this property. Furthermore, to fight against antibiotic resistance, emerging therapeutic approaches based on oxidative stress damage (e.g., metal ions, ROS generation) have received considerable attention and interest [38–42]. Typically, the generation of ROS to achieve antibacterial effects contradicts the bacterial growth environment, potentially causing secondary damage to local tissues. Excitingly, alkaline anions (OH⁻) can destroy the acidic growth environment preferred by most bacteria, disrupt the proton electrochemical gradient in the bacterial membrane space, and diminish the synthesis of ATP by excessive consumption of H^+, thus resulting in a remarkable decrease in bacteria [43–45]. Therefore, introducing alkaline drugs into the bacterial microenvironment could be an effective strategy for eliminating bacteria, and there is an urgent need to intelligently deliver alkaline drugs to deep infections caused by pathogenic bacteria.

Herein, aiming at overcoming the limitations of deep infections such as implantable osteomyelitis, the eddy-thermal effect of Mg implants under AMFs was applied to release H_2 and neutralize protons for anti-infection treatment and tissue repair (Scheme 1). Mg implants exhibited excellent H_2 generation under AMFs due to their eddy-thermal effect, which efficiently eliminated cytotoxic ROS and disturbed the sensitive environment of bacterial infection. In addition, the released OH⁻ anions caused an alkaline environment to deplete protons to inhibit bacterial proliferation, while the released H_2 further enhanced the
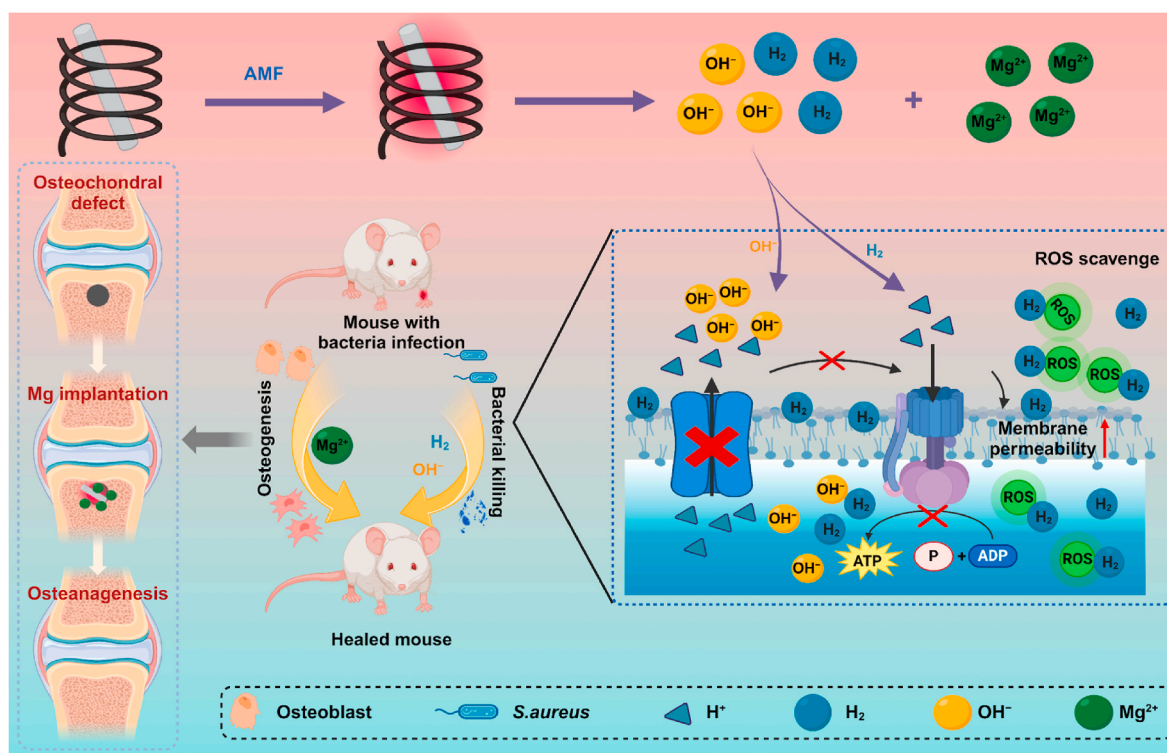
Scheme 1. Schematic illustration of synergistic Mg-mediated H_2 and proton depletion therapy for anti-infection treatment and tissue repair. Under an AMF, Mg implants in bone tissues release the therapeutic gas H_2 and ions (OH⁻ and Mg^{2+}) due to their excellent eddy-thermal effect. H_2 efficiently scavenges cytotoxic ROS for anti-inflammatory and damage the environment of bacteria. OH⁻ depletes protons in the bacterial microenvironment and inhibits bacterial energy metabolism. Subsequently, Mg^{2+} further promotes the healing of bone tissue, ultimately enabling efficient infection treatment and tissue repair.

permeability of the bacterial membrane and accelerated the entry of OH^- into the bacteria to kill them. The synergistic AMF-induced H_2 and proton depletion strategy not only killed both gram-negative and gram-positive bacteria but also effectively treated *S. aureus*-induced abscesses and osteomyelitis. In the case of osteomyelitis, Mg^{2+} released from Mg implants provided additional support for bone osteogenesis, thereby promoting the regeneration and growth of bone tissue. Overall, this work cleverly exploited the eddy-thermal effect and chemical activity of Mg implants under AMFs to reverse the inflammatory environment and suppress bacterial proliferation by simultaneously releasing therapeutic H_2 gas and functional ions (OH^- and Mg^{2+}), thus facilitating effective interventions for infection eradication and tissue repair. This simple and effective strategy highlights a novel approach for the treatment of deep tissue infection, thus presenting a promising avenue for clinical application.

2. Results and discussion

2.1. H_2 generation performance and ROS scavenging ability of Mg rods under AMFs

In accordance with Faraday's law of electromagnetic induction, macroscopic metallic conductors can engender thermal energy through eddy currents when subjected to an AMF, thus harboring significant potential for expediting responsive H_2 gas liberation [30,36]. Initially, a thorough exploration was conducted on the heating characteristics of Mg rods with different lengths and diameters under AMFs with different field intensities ($H_{appl} \times f_{appl} = M \times 10^9$ A m^{-1} s^{-1}, M = 2.4, 2.8, 3.2, 3.6, and 4.0) (Fig. 1a, Fig. S1). Notably, distinct temperature elevations in Mg rods were observed in a length- and diameter-dependent manner for 5 min under AMFs (Fig. 1b&c). Moreover, stronger eddy-thermal heating of the Mg rods was induced by higher field intensities of AMFs
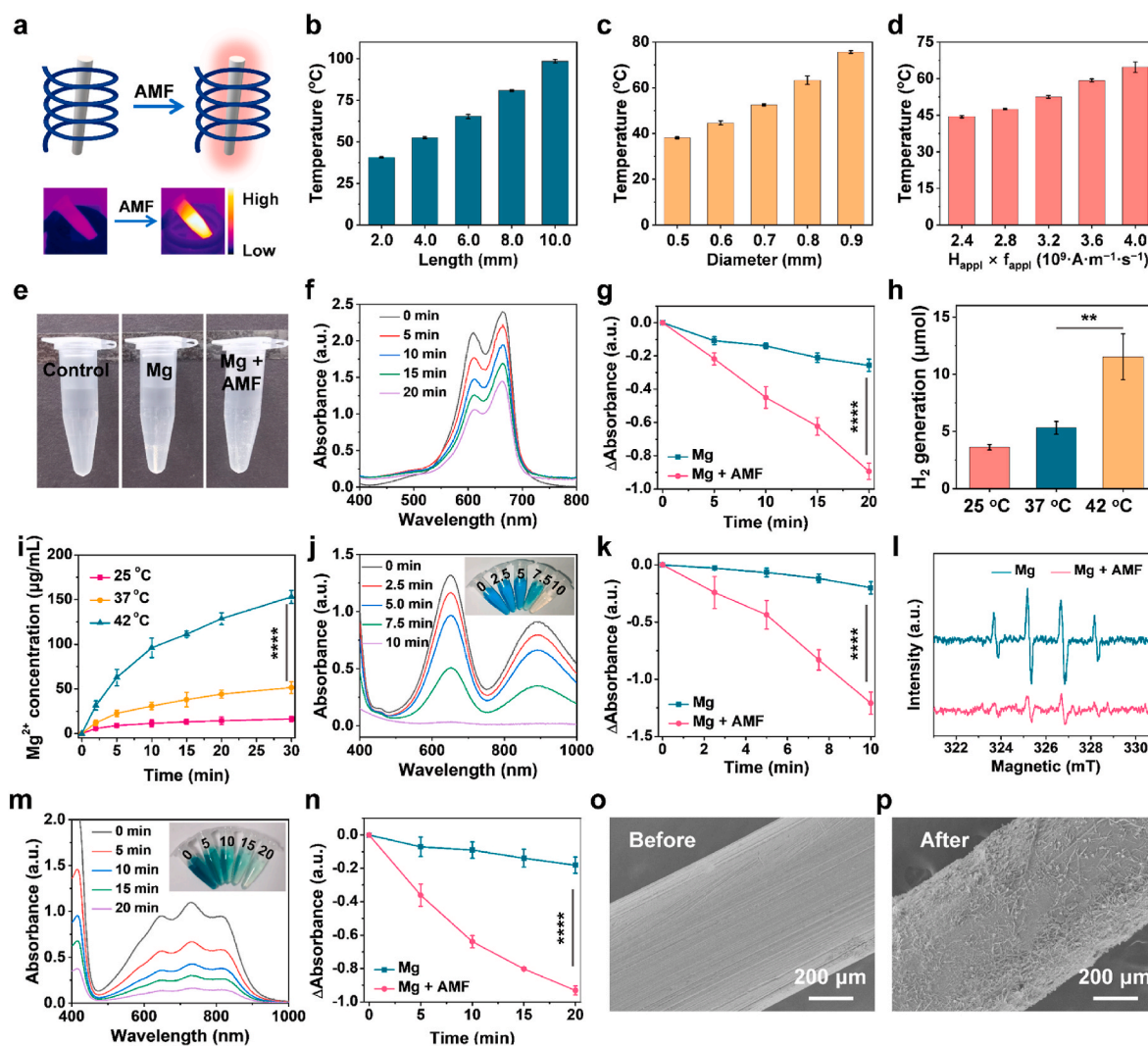

Fig. 1. H_2 generation performance and ROS scavenging ability of Mg rods under AMFs. (a) Schematic diagram showing the eddy-thermal effect of Mg implants under an AMF. **(b–d)** The temperature increase resulting from the eddy-thermal effect depended on the length (b), and diameter (c) of the Mg rods under different AMF intensities (d). **(e)** Photograph showing the H_2 generation in PBS from Mg with or without AMFs. **(f)** UV–vis absorption spectra of the MB solution containing Mg rods with an AMF after different times. **(g)** MB reduction properties of Mg rods with or without an AMF at different time. **(h)** H_2 generation performance of Mg rods in PBS at different temperatures. **(i)** Cumulative release of Mg^{2+} from Mg rods in PBS at different temperatures. **(j)** UV–vis absorption spectra of TMB after incubation with Fenton agents and Mg rods with an AMF after different times. **(k)** Comparison of •OH scavenging ability of Mg rods with or without an AMF at different time. **(l)** ESR spectra showing the •OH scavenging ability of Mg rods with or without an AMF. **(m)** UV–vis absorption spectra of •ABTS$^+$ radical after incubation of Mg rods with an AMF after different durations. **(n)** Comparison of the •ABTS$^+$ scavenging ability of Mg rods with or without an AMF at different time. **(o&p)** SEM images of Mg rods before (o) or after (p) being placed in an AMF. n = 3 independent samples. P values were calculated by the two-tailed student's t-test. **p < 0.01, and ****p < 0.0001.

(Fig. 1d, Fig. S2). In addition, the thermal effect of the AMFs on Mg rods was related to their relative orientation, with the most pronounced thermal impact observed when the AMF stood perpendicular to the maximal cross-sectional area of the Mg rods (Fig. S3). Indeed, by immersion in PBS, the Mg rods underwent a swift reaction with H_2O and generated copious H_2 bubbles under AMFs, while bare Mg rods scarcely generated visible bubbles (Fig. 1e). To confirm H_2 generation, methylene blue (MB) was utilized to detect H_2 generation from Mg rods with or without an AMF. The blue-colored MB rapidly undergoes a reduction reaction in the presence of H_2, resulting in the formation of a colorless MBH_2 compound [26,28]. Notably, the characteristic MB peak in the Mg + AMF group was notably diminished, while that in the bare Mg rod group was only slightly reduced, suggesting that the Mg rods generated more H_2 gas under AMFs by reacting with water (Fig. 1f&g, and Fig. S4). The H_2 generation from the Mg implants at different temperatures controlled by an AMF was quantitatively determined via gas chromatography (Fig. 1h). The quantity of H_2 generated by the Mg rods enhanced as the temperature increased. Meanwhile, the release of Mg^{2+}

from Mg rods was also gradually enhanced with the increasing temperature, thus fostering favorable conditions for subsequent biomedical applications (Fig. 1i). These findings validated that Mg rods had excellent eddy-thermal effect and controlled the release of H_2 under an AMF.

It is well known that H_2 gas has significant anti-inflammatory and antioxidant effects [17]. To assess the antioxidative capacity of H_2 gas generated by Mg rods under an AMF, two types of traditional radical probes were employed. First, the scavenging effects on •OH radicals generated by the Fenton reaction were evaluated using 3,3,5,5-tetramethylbenzidine (TMB) as an indicator of •OH. TMB, which was initially colorless, underwent oxidation in the presence of •OH, resulting in the formation of an oxTMB with blue color. When AMF was applied, H_2 produced by the Mg rods quickly altered the coloration of the oxTMB, whereas the pure Mg rods only induced a minor alteration in color (Fig. 1j&k, and Fig. S5). It was shown that AMF could expedite the release of H_2 from Mg rods to eliminate •OH radicals. Meanwhile, electron spin resonance (ESR) was also employed to reveal the excellent •OH (1: 2: 2: 1 signal) scavenging prowess of H_2 generated by the Mg
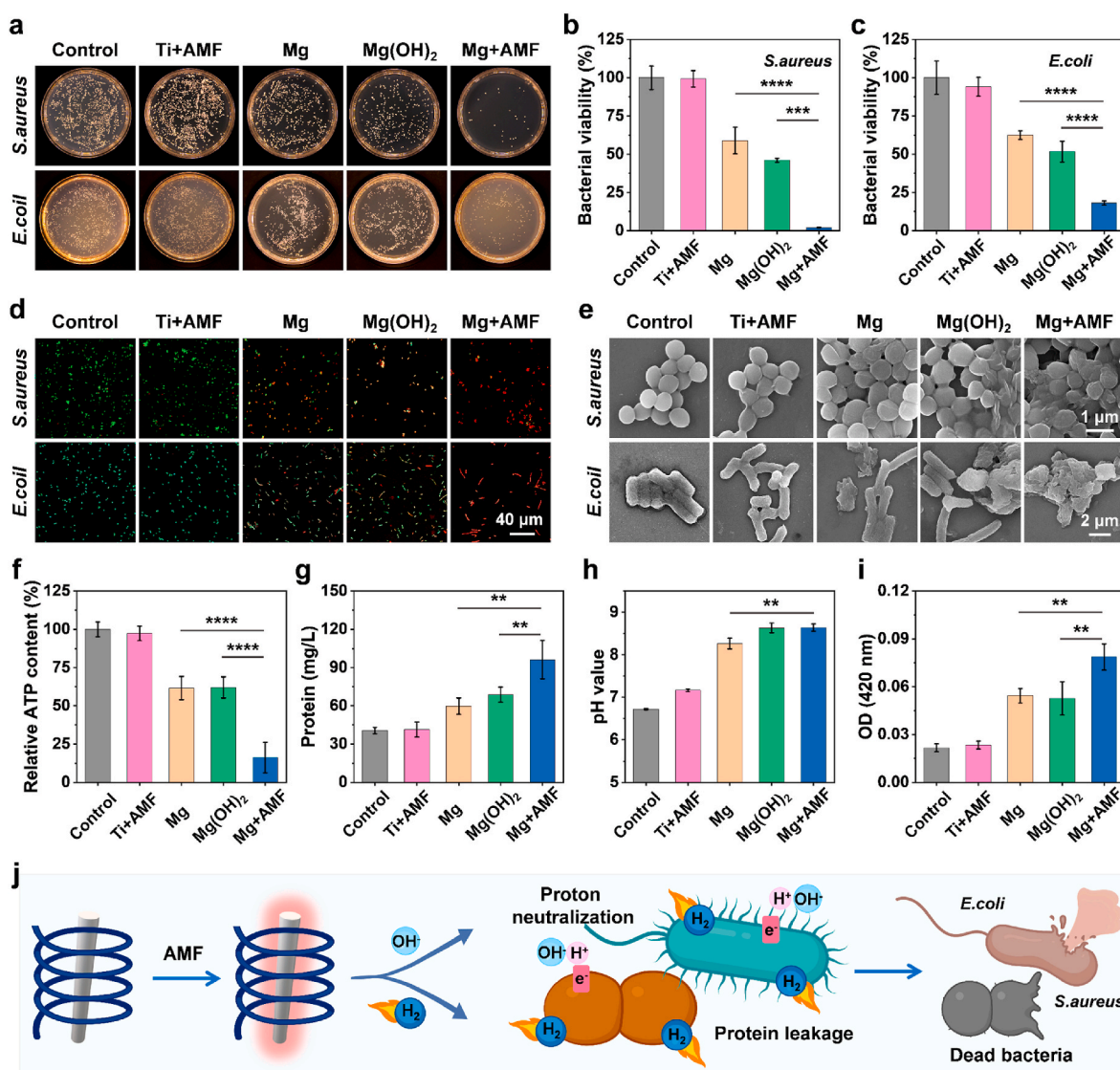
Fig. 2. *In vitro* **antibacterial ability and mechanism of Mg rods under AMFs. (a)** Representative photographs of bacterial (*E. coli* and *S. aureus*) colonies formed on LB-agar plates after various treatments. **(b&c)** Bacterial survival rate of *S. aureus* (b) and *E. coli* (c) after different treatments. **(d)** Confocal images of *S. aureus* and *E. coli* with live/dead staining after various treatments. **(e)** SEM images of *S. aureus* and *E. coli* post various treatments. **(f)** Relative ATP contents in *S. aureus* after various treatments. **(g)** Protein leakage evaluation of *S. aureus* after various treatments. **(h)** Changes in pH value after various treatments. **(i)** Changes in *S. aureus* cell membrane permeability determined by β-galactosidase. **(j)** The antibacterial mechanism of Mg rods under an AMF via H_2 and proton depletion. n = 5 biologically independent samples. P values were calculated by the one-way ANOVA with a Tukey post-hoc test. **p < 0.01, ***p < 0.001, and ****p < 0.0001.

rods under an AMF (Fig. 1l). Next, reactive nitrogen radicals (RNS, •ABTS$^+$ radicals) were utilized to measure the ability of Mg rods to scavenge RNS under an AMF (Fig. 1m&n, and Fig. S6). Notably, the decrease in •ABTS$^+$ absorbance following the introduction of Mg rods and exposure to AMFs suggested the pronounced capacity for RNS scavenging. Moreover, many corrosion marks appeared on the surface of the Mg rod implants after exposure to an AMF, suggesting a notable acceleration in the degradation of Mg due to the influence of AMF (Fig. 1o&p). By combining the exceptional H$_2$-donating properties of Mg rods with their responsiveness to AMFs, they proved to be remarkably effective scavengers of both ROS and RNS.

### 2.2. In vitro antibacterial ability and mechanism of Mg rods under AMFs

Encouraged by the excellent H$_2$ generation performance of the Mg rods under AMFs, the *in vitro* antibacterial efficacy of the Mg rods was subsequently evaluated against two prevalent bacterial strains associated with the majority of infections (gram-positive *S. aureus* and gram-negative *E. coli*). First, an assessment was conducted concerning the cytocompatibility and biodegradability of Mg rods *in vitro* (Fig. S7). Mg^{2+} showed low toxicity at concentrations up to 10 mM. In addition, the co-cultivation of cells with Mg rods demonstrated negligible cytotoxicity, indicating the remarkable biocompatibility of the Mg rods. The surface of the Mg implant became rough and uneven with increasing time, further corroborating its biodegradation (Fig. S8). Then, the antibacterial performance of Mg rods under AMFs was assessed through the analysis of colony-forming units (CFU) (Fig. 2a). Ti + AMF (heated to the same temperature with Mg, below 42 °C) and Mg(OH)$_2$ were used to explore the effects of temperature and pH, respectively. For gram-positive *S. aureus*, the bacterial survival rate of the Mg rods with AMF treatment group decreased to ~2.09 %, as opposed to a minor decrease to ~58.87 % for *S. aureus* treated with Mg rods alone (Fig. 2b). Moreover, a slight decrease occurred in the Mg(OH)$_2$-treated group (~46.06 %), demonstrating that an alkaline environment only partially inhibited the growth of bacteria. Moreover, there was no evident bactericidal ability against *S. aureus* in the Ti + AMF group, indicating that mild heat treatment (<42 °C) had no impact on bacterial activity. Additionally, a comparable trend was observed for gram-negative *E. coli* (Fig. 2c). In the absence of AMF, the viability of bacteria in the group treated with Mg rods exhibited a slight decrease to ~62.48 %. However, following the application of AMF, the survival rate of *E. coli* exhibited a pronounced tendency to decrease significantly, reaching ~18.12 %, further indicating the pivotal involvement of H$_2$ released by AMF in the antibacterial process. The variance in the inhibitory rate of Mg + AMF against *S. aureus* and *E. coli* may be related to the outer membranes on the surface of *E. coli*, which made them more difficult to kill [46]. To further confirm the antibacterial effects of Mg rods under AMFs, a live/dead bacterial viability kit was used to stain *S. aureus* and *E. coli* after different treatments (Fig. 2d). Mg rods or Mg(OH)$_2$ could induce bacterial death to a certain extent owing to their alkaline influence. In contrast, the Mg rods activated by AMF exhibited superior antibacterial performance, eliminating a significant number of bacteria. All these results verified the astonishingly broad-spectrum antibacterial efficacy of Mg rods subjected to AMF treatment. To highlight the contribution of H$_2$ more clearly, exogenous H$_2$ was used as an isolated variable to study its effect on bacteria (Figs. S9–11). H$_2$ merely exhibited a marginal inhibitory effect on bacterial proliferation but significantly changed the permeability of bacterial membranes. Therefore, H$_2$ mainly played an auxiliary role, by enhancing the permeability of bacterial membranes, and then accelerated the killing effect of alkaline condition on bacteria [20,47].

To elucidate the bacteriostatic mechanism, the different treated bacteria were immobilized, and their morphology was observed by scanning electron microscopy (SEM). The morphology of the bacteria in the control and Ti + AMF groups was complete and smooth, while the surface of bacteria in the Mg rod and Mg(OH)$_2$ groups exhibited a microscopic folding, indicating minor damage resulting from proton

consumption (Fig. 2e). Upon treatment with Mg rods plus AMF, many deformations and holes were produced on the surface of the bacteria. All these results confirmed that the abundant H$_2$ and OH$^-$ generated by Mg rods under AMF induced the rupture of the bacterial membrane, ultimately resulting in bacterial eradication. Given that OH$^-$ neutralizes the acidic milieu conducive to bacterial growth, thereby impeding ATP synthesis and inhibiting bacterial proliferation, the ATP concentration after different treatments was measured (Fig. 2f). It could be found that the ATP concentration of *S. aureus* decreased significantly under the combined action of AMF and Mg implants, indicating that bacterial activity was inhibited by the sustained generation of H$_2$ and OH$^-$. Moreover, protein leakage experiments were carried out to verify the antibacterial mechanism (Fig. 2g, Fig. S12). For the Ti + AMF treatment group, the protein leakage was negligible, further indicating that mild heat (<42 °C) did not have a noticeable effect on bacterial growth. Protein leakage occurred following the introduction of Mg rods or Mg(OH)$_2$, and the combination of Mg rods and AMF treatment resulted in abundant protein leakage. For both the *S. aureus* and *E. coli* treated with Mg rods plus AMF, the extent of protein leakage was greater than twice the amount observed in the groups treated with Mg rods or Mg(OH)$_2$. By analyzing the pH, it was determined that the pH level of the medium containing Mg rods was slightly increased after the AMF treatment (Fig. 2h). The effectiveness of Mg(OH)$_2$ under the same pH conditions was notably inferior to that of the combination of Mg with an AMF. Since H$_2$ can promote the destruction of cell membranes and expedite ion-induced harm, β-galactosidase was chosen as a metric for evaluating the permeability of the bacterial cell membrane [20,47]. Compared with those in the other groups, the Mg rods under AMF treatment exhibited a noticeable increase in the permeability of the bacterial membrane, thus expediting the ingress of OH$^-$ into bacterial, culminating in the efflux of cellular constituents and instigating bacterial demise (Fig. 2i). The aforementioned results indicated that Mg rods could achieve controllable generation of H$_2$ and OH$^-$ under AMFs to effectively eradicate bacteria (Fig. 2j). H$_2$ could inhibit the inflammatory environment in bacteria while enhancing the permeability of bacterial membranes. OH$^-$ functioned as a proton-consuming agent to impede the energy metabolism of bacteria. Simultaneously, H$_2$ disrupted the integrity of the bacterial membranes and accelerated the deleterious impact of OH$^-$ on the bacterial cells. Ultimately, the synergistic H$_2$ and proton depletion treatment effectively eradicated both gram-positive and gram-negative bacteria.

2.3. In vivo antibacterial ability against S. aureus-induced abscesses

Inspired by the *in vitro* remarkable antibacterial efficiency of Mg rods under AMFs, the *in vivo* antibacterial effect of synergistic H$_2$ and proton depletion treatment was further evaluated. *S. aureus*-induced subcutaneous abscess formation in mice was used to evaluate the *in vivo* antibacterial effect (Fig. 3a). The mice with abscesses were randomly divided into four groups, including the control, Ti + AMF, Mg alone, and Mg + AMF groups. For the Ti + AMF and Mg + AMF groups, the mice were subjected to AMF for 10 min, while ensuring that the temperature of the abscess tissues remained below 42 °C (Fig. S13). First, ultrasonic imaging was utilized to monitor the generation of H$_2$ in the abscess tissues, as the bubbles formed a strong contrast signal (Fig. 3b&c). Notably, when abscess tissues implanted with Mg rods were exposed to an AMF, strong ultrasonic signals appeared in the abscess tissues, indicating effective H$_2$ production. However, the ultrasound signals from Mg rod implanted tissues without an AMF were much weaker. At the same time as H$_2$ generation, other produced ions were expected to achieve therapeutic effects. Therefore, the pH of abscess tissues after different treatments was monitored by a pH microsensor (Fig. 3d). The results showed that after Mg rod implantation and exposure to an AMF, the acidity of the abscess locations transitioned toward alkaline condition, thereby fostering favorable conditions for infection treatment. In addition, *ex vivo* fluorescence imaging of the abscess sites after Mg rod
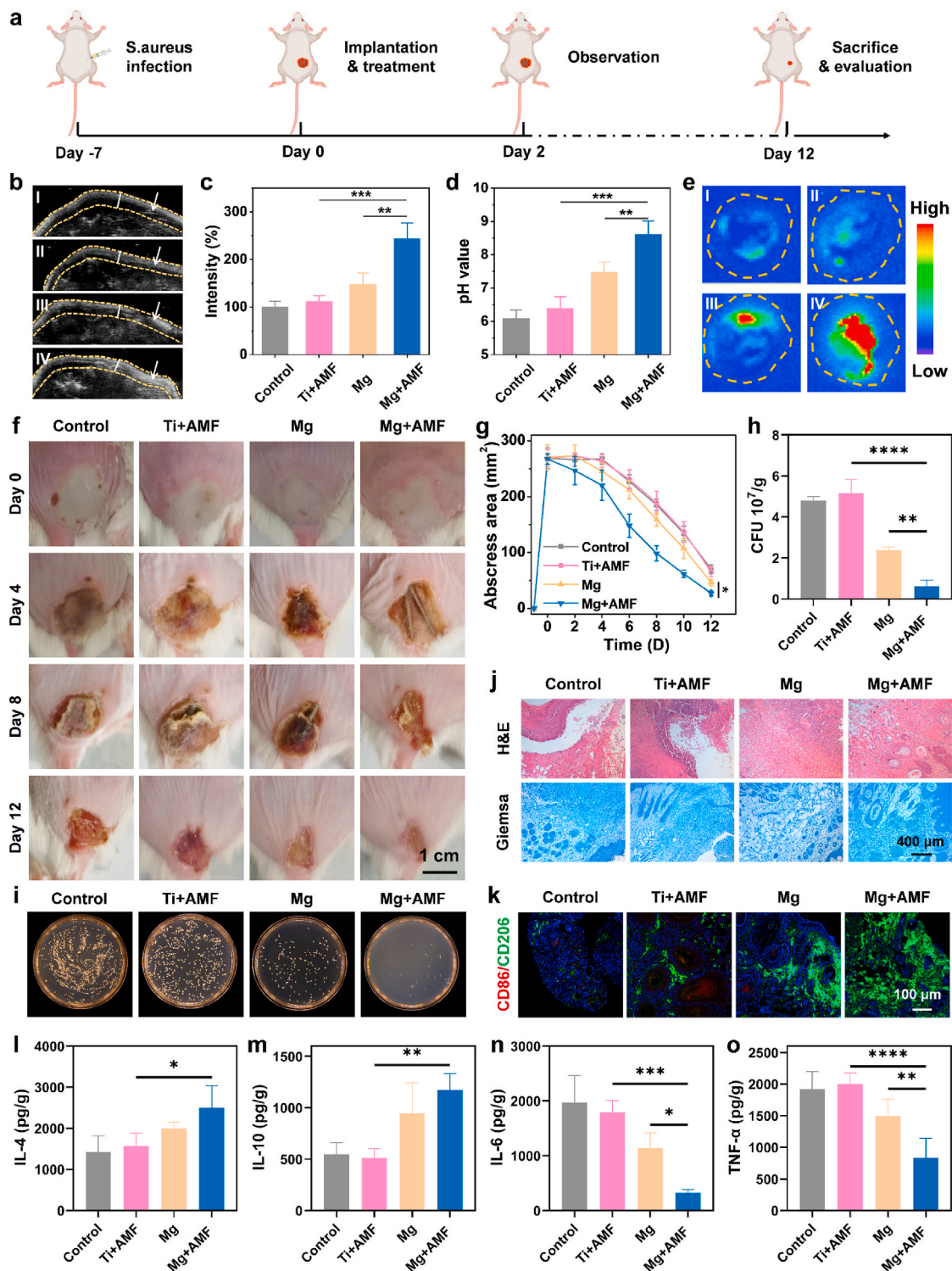
Fig. 3. *In vivo* **antibacterial capacity against** *S. aureus*-**induced abscesses. (a)** Schematic diagram of the *S. aureus* infection and treatment process. **(b&c)** *In vivo* ultrasonic imaging (b) and quantitative analysis (c) of the *S. aureus*-infected mice after different treatments (I: control, II: Ti + AMF, III: Mg, and IV: Mg + AMF). The arrows point to the abscess sites. **(d)** Change in the pH of abscess tissues in mice after different treatments. **(e)** *Ex vivo* fluorescence images of abscess tissues after different treatments (I: control, II: Ti + AMF, III: Mg, and IV: Mg + AMF). **(f)** Representative photographs of the *S. aureus*-infected mice were taken on days 0, 4, 8, and 12 after different treatments (control, Ti + AMF, Mg, and Mg + AMF). **(g)** The variation curves of the abscess area in mice after different treatments. **(h)** Quantitative analysis of surviving bacteria collected from the *S. aureus*-infected tissues. **(i)** Representative images of *S. aureus* colonies formed on LB-agar plates from the skin tissues of *S. aureus*-infected sites on day 4 after different treatments (control, Ti + AMF, Mg, and Mg + AMF). **(j)** Microscopy images of H&E- and Giemsa-stained skin slices collected from mice on day 8 after various treatments. **(k)** Immunofluorescence staining images of CD86 and CD206-stained skin sections. **(l–o)** IL-4 (l), IL-10 (m), IL-6 (n), and TNF-α (o) levels in *S. aureus*-induced abscesses from various groups. n = 4 biologically independent animals. P values were calculated by the two-tailed student's t-test. *p < 0.05, **p < 0.01, ***p < 0.001, and ****p < 0.0001.

implantation using a pH-responsive fluorescence probe showed the same trend (Fig. 3e). According to the experimental results, mice treated with Mg rods under an AMF exhibited improved and accelerated recovery, as indicated by the decreased size of the abscess area after treatment (Fig. 3f&g). The sole implantation of Mg demonstrated modest efficacy in diminishing the abscess area, and the combination of Ti with AMF had a marginal influence on abscess progression. To further evaluate the antibacterial efficacy of Mg rods under AMFs, the residual bacteria in the treated abscess tissue were evaluated (Fig. 3h&i). The infected tissues were weighed and homogenized to quantify the degree of bacterial infiltration. The Mg rods plus AMF exhibited superior antibacterial performance, eliminating a significant number of bacteria. To further evaluate the efficacy of various treatments on tissue healing, immuno-histochemical analysis was performed on the dermal tissue surrounding the abscess area in mice (Fig. 3j). Hematoxylin and eosin (H&E) and Giemsa staining revealed that the abscess sites treated with Mg rods combined with AMF exhibited superior recovery compared with those in the remaining groups. These findings collectively suggested that synergistic Mg-mediated H_2 and proton neutralization therapy rapidly eradicated bacteria within abscess sites and expedited the tissue healing process.

Next, M2-type macrophages can accelerate the regeneration of collagens and new blood vessels and thus significantly affect tissue regeneration [48,49]. Thus, the infiltration of macrophages inside the abscess sites was further evaluated (Fig. 3k). The M2 phenotype macrophages exhibited substantial augmentation within the tissues of the Mg + AMF group, indicating a significant acceleration of skin wound healing via immune cell infiltration around these abscesses. Moreover, the number of M1-type proinflammatory macrophages was decreased, indicating the importance of H_2 generated by Mg plus AMF treatment for the regulation of tissue healing. To further validate the changes in the inflammatory environment, the levels of anti-inflammatory cytokines and pro-inflammatory cytokines around abscess tissues were evaluated (Fig. 3l-o). In the Mg + AMF group, there was a decrease in the expression of pro-inflammatory cytokines, including tumor necrosis factor-α (TNF-α) and interleukin-6 (IL-6), and an increase in the production of anti-inflammatory cytokines, including IL-4 and IL-10. These results confirmed that synergistic Mg-mediated H_2 and proton neutralization therapy effectively eradicated bacteria, reversed the inflammatory microenvironment, and thereby facilitated the wound healing process. Furthermore, no discernible histological damage was observed in the organ sections obtained from the mice subjected to Mg + AMF treatment (Fig. S14). Other indicators were further performed to determine the potential occurrence of side effects induced by this strategy. The levels of alanine aminotransferase (ALT), aspartic amino-transferase (AST), albumin (ALB), and alkaline phosphatase (ALP), which are vital indicators of liver function, were similar to those of the control group and were all within the reference range (Fig. S15). This suggested that synergistic therapy facilitated by Mg rods did not cause any notable hepatotoxic effects. Uric acid (UA) levels, an indicator of kidney function, were also within the normal range. In terms of hematological evaluation, various factors, including the white blood cells (WBC), red blood cells (RBC), hemoglobin (HGB), hematocrit (HCT), mean corpuscular volume (MCV), mean corpuscular hemoglobin (MCH), mean corpuscular hemoglobin concentration (MCHC), and platelets (PLT) were performed (Fig. S16). Compared with the control group, all hematological indexes of the Mg + AMF group were normal. Overall, all the above results collectively demonstrated that the synergistic effect of Mg-mediated H_2 and proton neutralization therapeutic strategy caused no obvious toxicity to the treated animals.
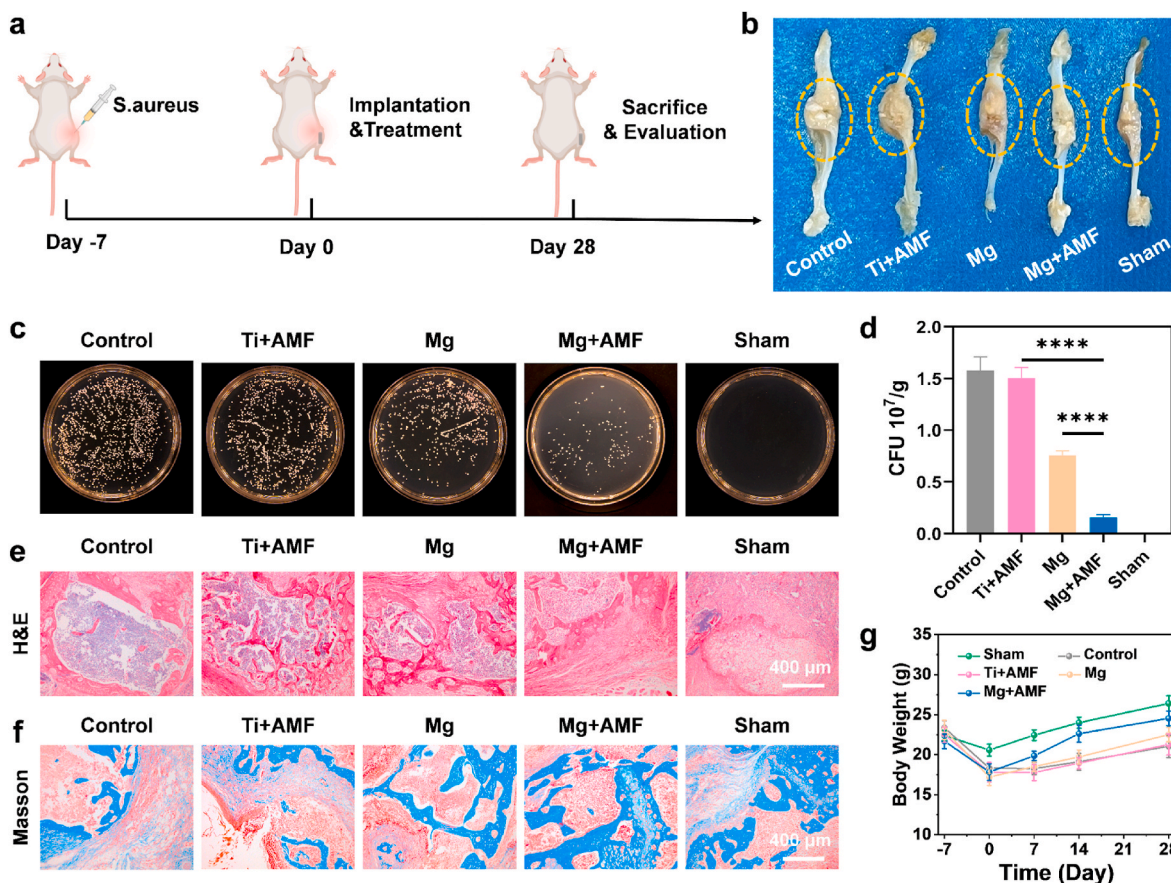
2.4. In vivo antibacterial effect against osteomyelitis

Since AMF is not limited by the depth of tissue penetration, the antibacterial efficacy of Mg rods in combination with AMF for combating *S. aureus* infection in osteomyelitis models was further explored (Fig. 4a). After a 7-day period following infection by *S. aureus*, an obvious swelling in the surgical area was observed, indicating that the osteomyelitis model was successfully induced. Bone tissues were removed at the end of treatment to evaluate the effectiveness of the therapeutic approach. Compared to those in the sham group, significant swelling and ulceration occurred in the control and Ti + AMF groups, suggesting severe bacterial infection accompanied by inflammation (Fig. 4b). However, the swelling and ulceration were reduced in the Mg group and significantly relieved in the Mg + AMF group. To further verify the antibacterial ability of the Mg rods under AMF, the remaining bacteria in the infected bone tissues after treatment were evaluated (Fig. 4c&d). The mice were sacrificed after 7 days, after which abscess tissues were dissected to evaluate antibacterial ability. Mg implantation resulted in antibacterial activity, whereas this antibacterial activity substantially increased after AMF application. These results confirmed that the synergistic Mg-mediated H_2 and proton neutralization therapy exhibited remarkable efficacy in eliminating osteomyelitis. H&E and Masson staining were also performed to evaluate the extent of bone tissue healing surrounding the infected sites (Fig. 4e&f). In the control group and the Ti + AMF group, there were some bone defects and a small amount of collagen at the sites of infection. Remarkably, the bone tissues of the Mg + AMF group were well repaired, with greater deposition of fresh collagen surrounding the sites of the bone defect. Furthermore, during the initial stages of infection, there was a notable downward trend in the body weights (Fig. 4g). However, this trend soon eased up in the Mg + AMF group, as indicated by a noteworthy increase in weight beginning on the 7th day. In addition, there was no obvious histological damage of major organs in the Mg + AMF group (Fig. S17). Taken together, these findings confirmed that the synergistic Mg-mediated H_2 and proton neutralization therapy efficiently eradicated osteomyelitis and accelerated the repair of bone tissues.

2.5. Osteogenesis behavior assessment

Mg^{2+} strongly facilitates the process of bone regeneration by amplifying the mineralization of the matrix and the expression of genes and proteins associated with osteogenesis [50–52]. The release of Mg^{2+} was first measured (Fig. S18), and then the osteogenic ability of the mouse osteoblastic cell line MC3T3-E1 was investigated. After treatment with Mg rods under AMF, the staining and activity of alkaline phosphatase revealed substantial increases in both the expression and activity of these enzymes (Fig. 5a&b). The application of alizarin red staining further revealed an increase in the presence of calcium nodules within the Mg rod treated groups following prolonged induction (Fig. 5c&d). These results confirmed that the Mg^{2+} released from Mg rods under AMF could efficiently promote bone regeneration *in vitro*. Furthermore, micro-CT was used to evaluate the repair ability of the bone tissues after the different treatments (Fig. 5e). Obvious bone defects were observed in both the control and Ti + AMF groups, while the Mg rods had some healing effects. Obviously, an accelerated healing trend was observed in the Mg + AMF group, which was attributed to the release of Mg^{2+} and the healthy environment induced by H_2, thus enhancing bone regeneration. To provide a more comprehensive evaluation of the density and strength of the newly formed bone, several crucial parameters were meticulously assessed, including the bone volume/total volume (BV/TV), bone mineral density (BMD), trabecular separation (Tb. Sp), trabecular number (Tb. N), and trabecular thickness (Tb. Th) (Fig. 5f–j). The Mg + AMF group exhibited superior BV/TV, BMD, Tb. Th, and Tb. N but exhibited a decreased Tb. Sp compared to those of the control group, suggesting the presence of a newer bone mass characterized by enhanced strength, thicker trabecular plates, and heightened trabecular density. Overall, since AMFs are not limited by the depth of tissue penetration, this strategy effectively prevented bone destruction caused by *S. aureus*-induced osteomyelitis.

Fig. 4. *In vivo* **antibacterial effect against osteomyelitis. (a)** Schematic diagram of the *S. aureus* infection and treatment process. **(b)** Representative photographs of the *S. aureus*-infected sites after different treatments. **(c)** Representative images of *S. aureus* colonies formed on LB agar plates from the bone tissues of *S. aureus*-infected sites after different treatments (control, Ti + AMF, Mg, Mg + AMF, and Sham). **(d)** Quantitative analysis of surviving bacteria collected from the *S. aureus*-infected sites. **(e&f)** H&E (e) and Masson (f) staining of infected bone tissue slices. **(g)** Body weight variation of the mice after different treatments. n = 3 biologically independent animals. P values were calculated by the two-tailed student's t-test. ****p < 0.0001.

3. Conclusion

In summary, the eddy-thermal effect of Mg implants under AMFs was used to release H_2 and deplete protons for the treatment of infections and regeneration of tissues. Mg implants exhibited excellent H_2 generation performance under AMFs, thus offering an efficient solution to counteract cytotoxic ROS and disrupt the sensitive environment of bacterial infection. Moreover, the released OH^- consumed protons in the microenvironment, thus impeding the energy metabolism of bacteria to inhibit bacterial proliferation. Moreover, the released H_2 further enhanced the bacterial membrane permeability and accelerated the damage caused by OH^-. This synergistic AMF-induced H_2 and proton depletion strategy not only killed both gram-positive and gram-negative bacteria, but also be employed for effective and accurate treatment of *S. aureus*-induced abscesses and osteomyelitis *in vivo*. Especially in osteomyelitis, Mg^{2+} released from Mg implants further promoted bone osteogenesis. Overall, our work cleverly exploited the eddy-thermal effect and chemical activity of Mg implants under AMFs to reverse the inflammatory environment and suppress bacterial proliferation, achieved by the synchronous release of therapeutic H_2 and functional ions (OH^- and Mg^{2+}), ultimately enabling efficient infection treatment and tissue repair. The strategy of accomplishing multiple objectives with a single endeavor is both simple and efficacious, providing us with a fresh perspective for addressing the intricacies of deep tissue infection, thus highlighting its potential for clinical application.

Attributing to the excellent thermal conductivity inherent in Mg implants, it is meaningful to control the temperature throughout the procedure to produce therapeutic H_2 gas and functional ions (OH^- and Mg^{2+}). However, the location and orientation of the Mg implant would affect its heating effect and thus affect the treatment effect. Therefore, in future practical applications, clinical equipment such as magnetic resonance imaging (MRI) and computerized tomography (CT) imaging can be used to accurately locate the lesion tissues and implant locations. Moreover, achieving the definitive translation of the technology remains challenging. This arises due to the juxtaposition of utilizing swift-reacting Mg implant byproducts for therapeutic interventions, where the mechanical properties and therapeutic functions will conflict. Perhaps the clever amalgamation of Mg with other metal implants with superior mechanical properties, such as Ti implants, represents an ideal strategy. In general, addressing deep tissue infections in the future through minimally invasive implantation of micro Mg implants or composite implants infused with Mg holds profound significance. In conclusion, our proposed synergistic AMF-induced H_2 and proton depletion strategy based on Mg implants offers new opportunities for the treatment of osteomyelitis and other deep tissue infections.
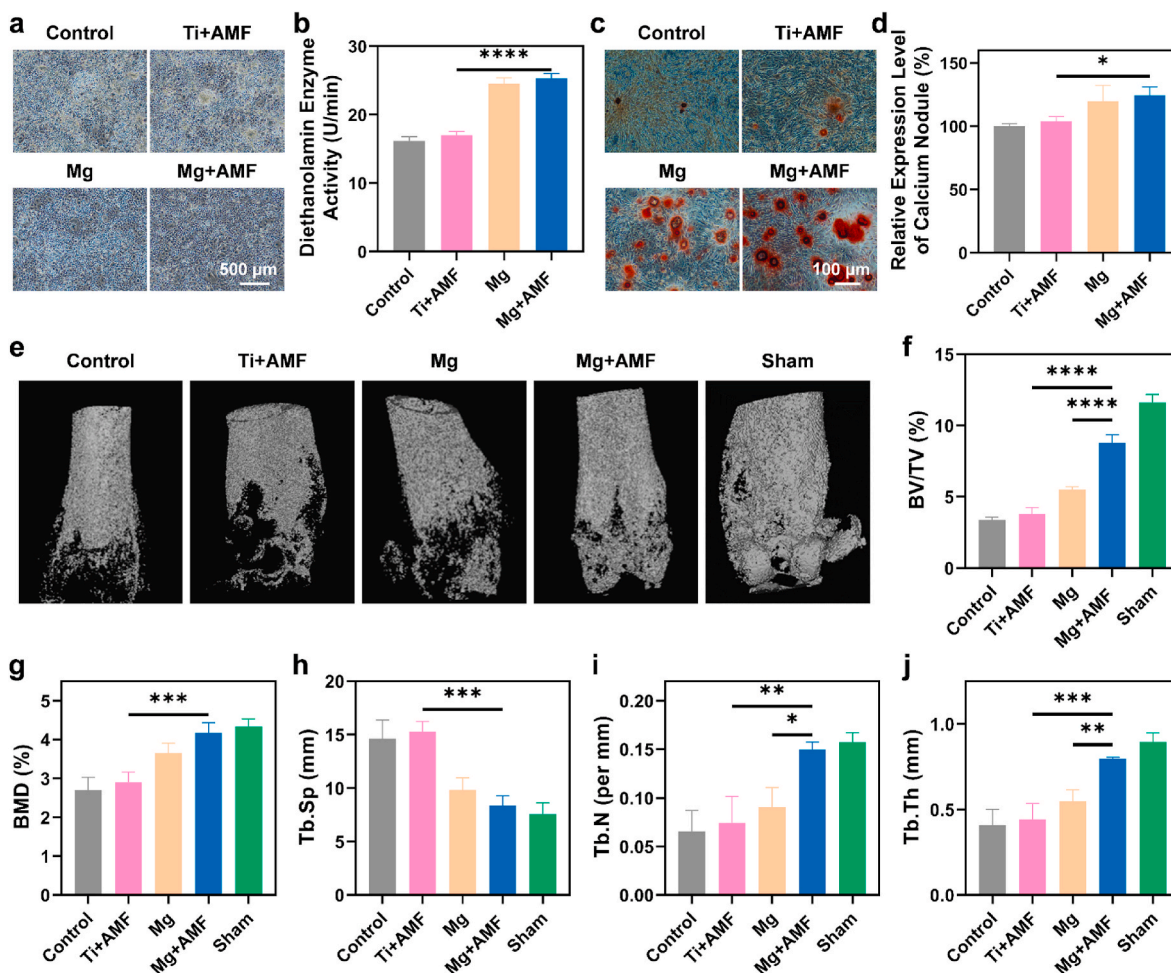
Ethics approval and consent to participate

Ethics Committee (Soochow University Laboratory Animal Center) has approved the animal experiments.

Competing interests

All authors declare no competing financial interest.

Fig. 5. Osteogenesis behavior assessment. **(a&b)** Alkaline phosphatase staining (a) and activity (b) of MC3T3-E1 cells after 7 days of osteogenic induction. **(c)** Alizarin red staining of MC3T3-E1 cells after 14 days of osteogenic differentiation. **(d)** Quantitative analysis of alizarin red staining. **(e)** Three-dimensional reconstruction of infected bone tissues from various treatment groups. **(f–j)** Quantification of the BV/TV (f), BMD (g), Tb. Sp (h), Tb. N (i), and Tb. Th (j) in (e). n = 3 biologically independent animals. P values were calculated by the two-tailed student's t-test. *$p < 0.05$, **$p < 0.01$, ***$p < 0.001$, and ****$p < 0.0001$.

CRediT authorship contribution statement

Nailin Yang: Writing – original draft, Formal analysis, Data curation. **Xiaoyuan Yang:** Formal analysis, Data curation. **Shuning Cheng:** Formal analysis, Data curation. **Xiang Gao:** Formal analysis, Data curation. **Shumin Sun:** Formal analysis. **Xuan Huang:** Formal analysis. **Jun Ge:** Formal analysis. **Zhihui Han:** Formal analysis. **Cheng Huang:** Formal analysis. **Yuanjie Wang:** Formal analysis. **Chong Cheng:** Resources. **Liang Cheng:** Writing – review & editing, Validation, Supervision, Project administration, Funding acquisition.

Declaration of competing interest

The authors declare that they have no known competing financial interests or personal relationships that could have appeared to influence the work reported in this paper.

Acknowledgements

Appendix A. Supplementary data

Supplementary data to this article can be found online at https://doi.org/10.1016/j.bioactmat.2024.05.010.

References

[1] S. Baker, N. Thomson, F.-X. Weill, K.E. Holt, Genomic insights into the emergence and spread of antimicrobial-resistant bacterial pathogens, Science 360 (6390) (2018) 733–738.

[2] T. Mestrovic, G.R. Aguilar, L.R. Swetschinski, K.S. Ikuta, A.P. Gray, N.D. Weaver, C. Han, E.E. Wool, A.G. Hayoon, S.I. Hay, The burden of bacterial antimicrobial resistance in the WHO European region in 2019: a cross-country systematic analysis, Lancet Public Health 7 (11) (2022) e897–e913.

[3] J. Ma, C. Wu, Bioactive inorganic particles-based biomaterials for skin tissue engineering, Explorations 2 (5) (2022) 20210083.

[4] J. Li, X. Liu, Y. Zheng, Z. Cui, H. Jiang, Z. Li, S. Zhu, S. Wu, Achieving Fast Charge separation by ferroelectric ultrasonic interfacial engineering for rapid sonotherapy of bacteria-infected osteomyelitis, Adv. Mater. 35 (13) (2023) 2210296.

[5] Y. Ren, J. Weeks, T. Xue, J. Rainbolt, K.L. de Mesy Bentley, Y. Shu, Y. Liu, E. Masters, P. Cherian, C.E. McKenna, Evidence of bisphosphonate-conjugated sitafloxacin eradication of established methicillin-resistant S. aureus infection with osseointegration in murine models of implant-associated osteomyelitis, Bone Res. 11 (1) (2023) 51.

[6] Y. Bian, T. Hu, Z. Lv, Y. Xu, Y. Wang, H. Wang, W. Zhu, B. Feng, R. Liang, C. Tan, Bone tissue engineering for treating osteonecrosis of the femoral head, Explorations 3 (2) (2023) 20210105.

[7] W. Li, F. Separovic, N.M. O'Brien-Simpson, J.D. Wade, Chemically modified and conjugated antimicrobial peptides against superbugs, Chem. Soc. Rev. 50 (8) (2021) 4932–4973.

[8] T.-Y. Park, J. Jeon, N. Lee, J. Kim, B. Song, J.-H. Kim, S.-K. Lee, D. Liu, Y. Cha, M. Kim, Co-transplantation of autologous Treg cells in a cell therapy for Parkinson's disease, Nature 619 (7970) (2023) 606–615.

[9] Z. Zhang, R. Dalan, D. Hu, J.W. Wang, N.W. Chew, K.K. Poh, R.S. Tan, T.W. Soong, Y. Dai, L. Ye, Reactive oxygen species scavenging nanomedicine for the treatment of ischemic heart disease, Adv. Mater. 34 (35) (2022) 2202169.

[10] H. Zhao, J. Huang, Y. Li, X. Lv, H. Zhou, H. Wang, Y. Xu, C. Wang, J. Wang, Z. Liu, ROS-scavenging hydrogel to promote healing of bacteria infected diabetic wounds, Biomaterials 258 (2020) 120286.

[11] N. Yang, F. Gong, L. Cheng, Recent advances in upconversion nanoparticle-based nanocomposites for gas therapy, Chem. Sci. 13 (7) (2022) 1883–1898.

[12] L. Yu, P. Hu, Y. Chen, Gas-generating nanoplatforms: material chemistry, multifunctionality, and gas therapy, Adv. Mater. 30 (49) (2018) 1801964.

[13] Y. Wang, T. Yang, Q. He, Strategies for engineering advanced nanomedicines for gas therapy of cancer, Natl. Sci. Rev. 7 (9) (2020) 1485–1512.

[14] Y. Opoku-Damoah, R. Zhang, H.T. Ta, Z.P. Xu, Therapeutic gas-releasing nanomedicines with controlled release: advances and perspectives, Explorations 2 (5) (2022) 20210181.

[15] Z. Su, L. Kong, Y. Dai, J. Tang, J. Mei, Z. Qian, Y. Ma, Q. Li, S. Ju, J. Wang, Bioresponsive nano-antibacterials for H$_2$S-sensitized hyperthermia and immunomodulation against refractory implant–related infections, Sci. Adv. 8 (14) (2022) eabn1701.

[16] N. Yang, F. Gong, B. Liu, Y. Hao, Y. Chao, H. Lei, X. Yang, Y. Gong, X. Wang, Z. Liu, Magnesium galvanic cells produce hydrogen and modulate the tumor microenvironment to inhibit cancer growth, Nat. Commun. 13 (1) (2022) 2336.

[17] Y. Wu, M. Yuan, J. Song, X. Chen, H. Yang, Hydrogen gas from inflammation treatment to cancer therapy, ACS Nano 13 (8) (2019) 8505–8511.

[18] Y. You, Y.-X. Zhu, J. Jiang, M. Wang, Z. Chen, C. Wu, J. Wang, W. Qiu, D. Xu, H. Lin, Water-enabled H$_2$ generation from hydrogenated silicon nanosheets for efficient anti-inflammation, J. Am. Chem. Soc. 144 (31) (2022) 14195–14206.

[19] N. Matei, R. Camara, J.H. Zhang, Emerging mechanisms and novel applications of hydrogen gas therapy, Med. Gas Res. 8 (3) (2018) 98.

[20] W. Zhang, Y. Zhou, Y. Fan, R. Cao, Y. Xu, Z. Weng, J. Ye, C. He, Y. Zhu, X. Wang, Metal–organic-framework-based hydrogen-release platform for multieffective Helicobacter pylori targeting therapy and intestinal flora protective capabilities, Adv. Mater. 34 (2) (2022) 2105738.

[21] S. Yu, G. Li, P. Zhao, Q. Cheng, Q. He, D. Ma, W. Xue, NIR-laser-controlled hydrogen-releasing PdH nanohydride for synergistic hydrogen-photothermal antibacterial and wound-healing therapies, Adv. Funct. Mater. 29 (50) (2019) 1905697.

[22] G. Zhou, E. Goshi, Q. He, Micro/Nanomaterials-augmented hydrogen therapy, Adv. Healthcare Mater. 8 (16) (2019) 1900463.

[23] H. Ding, F. Ren, P. Liu, Y. Feng, X. Ma, Z. Shen, Q. Shi, M. Xu, W. Li, H. Chen, Cu^{2+}-Anchored Carbon nano-photocatalysts for visible water splitting to boost hydrogen cuproptosis, Angew. Chem., Int. Ed. 62 (44) (2023) e202311549.

[24] G. Qi, T. Yu, J. Li, Z. Guo, K. Ma, Y. Jin, Imaging guided endogenic H$_2$-augmented electrochemo-sonodynamic domino Co-therapy of tumor in vivo, Adv. Mater. 35 (9) (2023) 2208414.

[25] F. Gong, J. Xu, B. Liu, N. Yang, L. Cheng, P. Huang, C. Wang, Q. Chen, C. Ni, Z. Liu, Nanoscale CaH$_2$ materials for synergistic hydrogen-immune cancer therapy, Chem 8 (1) (2022) 268–286.

[26] P. Zhao, Z. Jin, Q. Chen, T. Yang, D. Chen, J. Meng, X. Lu, Z. Gu, Q. He, Local generation of hydrogen for enhanced photothermal therapy, Nat. Commun. 9 (1) (2018) 4241.

[27] S. Chen, Y. Zhu, Q. Xu, Q. Jiang, D. Chen, T. Chen, X. Xu, Z. Jin, Q. He, Photocatalytic glucose depletion and hydrogen generation for diabetic wound healing, Nat. Commun. 13 (1) (2022) 5684.

[28] M. Yuan, S. Liang, L. Yang, F. Li, B. Liu, C. Yang, Z. Yang, Y. Bian, P.a. Ma, Z. Cheng, Rational design of platinum–bismuth sulfide Schottky heterostructure for sonocatalysis-mediated hydrogen therapy, Adv. Mater. 35 (10) (2023) 2209589.

[29] Q. Xu, S. Chen, L. Jiang, C. Xia, L. Zeng, X. Cai, Z. Jin, S. Qin, W. Ding, Q. He, Sonocatalytic hydrogen/hole-combined therapy for anti-biofilm and infected diabetic wound healing, Natl. Sci. Rev. 10 (5) (2023) nwad063.

[30] N. Yang, X. Sun, Y. Zhou, X. Yang, J. You, Z. Yu, J. Ge, F. Gong, Z. Xiao, Y. Jin, Liquid metal microspheres with an eddy-thermal effect for magnetic hyperthermia-enhanced cancer embolization-immunotherapy, Sci. Bull. 68 (16) (2023) 1772–1783.

[31] H. Gavilán, S.K. Avugadda, T. Fernández-Cabada, N. Soni, M. Cassani, B.T. Mai, R. Chantrell, T. Pellegrino, Magnetic nanoparticles and clusters for magnetic hyperthermia: optimizing their heat performance and developing combinatorial therapies to tackle cancer, Chem. Soc. Rev. 50 (20) (2021) 11614–11667.

[32] Y. Zhu, Q. Li, C. Wang, Y. Hao, N. Yang, M. Chen, J. Ji, L. Feng, Z. Liu, Rational design of biomaterials to potentiate cancer thermal therapy, Chem. Rev. 123 (11) (2023) 7326–7378.

[33] L. Wang, P. Hu, H. Jiang, J. Zhao, J. Tang, D. Jiang, J. Wang, J. Shi, W. Jia, Mild hyperthermia-mediated osteogenesis and angiogenesis play a critical role in magnetothermal composite-induced bone regeneration, Nano Today 43 (2022) 101401.

[34] X. Yang, N. Yang, L. Zhang, D. Zhao, H. Lei, S. Cheng, J. Ge, X. Ma, C. Ni, Z. Liu, Eddy current thermal effect based on magnesium microrods for combined tumor therapy, Chem. Eng. J. 446 (2022) 137038.

[35] R. Zaman, X. Cai, Q.T. Shubhra, Hyperthermia–embolization–immunotherapy: a potent trio in advancing cancer treatment, Trends Mol. Med. 29 (12) (2023) 976–978.

[36] N. Yang, F. Gong, L. Cheng, H. Lei, W. Li, Z. Sun, C. Ni, Z. Wang, Z. Liu, Biodegradable magnesium alloy with eddy thermal effect for effective and accurate magnetic hyperthermia ablation of tumors, Natl. Sci. Rev. 8 (1) (2021) nwaa122.

[37] J. Ge, N. Yang, Y. Yang, H. Yu, X. Yang, T. Wang, S. Cheng, Y. Wang, Z. Han, The combination of eddy thermal effect of biodegradable magnesium with immune checkpoint blockade shows enhanced efficacy against osteosarcoma, Bioact. Mater. 25 (2023) 73–85.

[38] J.M.V. Makabenta, A. Nabawy, C.-H. Li, S. Schmidt-Malan, R. Patel, V.M. Rotello, Nanomaterial-based therapeutics for antibiotic-resistant bacterial infections, Nat. Rev. Microbiol. 19 (1) (2021) 23–36.

[39] C. Mao, W. Jin, Y. Xiang, Y. Zhu, J. Wu, X. Liu, S. Wu, Y. Zheng, K.M. Cheung, K.W. K. Yeung, Realizing highly efficient sonodynamic bactericidal capability through the phonon–electron coupling effect using two-dimensional catalytic planar defects, Adv. Mater. 35 (9) (2023) 2208681.

[40] M. Godoy-Gallardo, U. Eckhard, L.M. Delgado, Y.J. de Roo Puente, M. Hoyos-Nogués, F.J. Gil, R.A. Perez, Antibacterial approaches in tissue engineering using metal ions and nanoparticles: from mechanisms to applications, Bioact. Mater. 6 (12) (2021) 4470–4490.

[41] C.H. Goss, Y. Kaneko, L. Khuu, G.D. Anderson, S. Ravishankar, M.L. Aitken, N. Lechtzin, G. Zhou, D.M. Czyz, K. McLean, Gallium disrupts bacterial iron metabolism and has therapeutic effects in mice and humans with lung infections, Sci. Transl. Med. 10 (460) (2018) eaat7520.

[42] S. Cheng, L. Chen, F. Gong, X. Yang, Z. Han, Y. Wang, J. Ge, X. Gao, Y. Li, X. Zhong, PtCu nanosonosensitizers with inflammatory microenvironment regulation for enhanced sonodynamic bacterial elimination and tissue repair, Adv. Funct. Mater. 33 (22) (2023) 2212489.

[43] Y. Xue, L. Zhang, F. Liu, F. Dai, L. Kong, D. Ma, Y. Han, Alkaline "nanoswords" coordinate ferroptosis-like bacterial death for antibiosis and osseointegration, ACS Nano 17 (3) (2023) 2711–2724.

[44] M. Li, L. Nan, C. Liang, Z. Sun, L. Yang, K. Yang, Antibacterial behavior and related mechanisms of martensitic Cu-bearing stainless steel evaluated by a mixed infection model of Escherichia coli and Staphylococcus aureus in vitro, J. Mater. Sci. Technol. 62 (2021) 139–147.

[45] J. Tan, D. Wang, H. Cao, Y. Qiao, H. Zhu, X. Liu, Effect of local alkaline microenvironment on the behaviors of bacteria and osteogenic cells, ACS Appl. Mater. Interfaces 10 (49) (2018) 42018–42029.

[46] N.C. Rosas, T. Lithgow, Targeting bacterial outer-membrane remodelling to impact antimicrobial drug resistance, Trends Microbiol. 30 (6) (2022) 544–552.

[47] J. Zhou, E. Karshalev, R. Mundaca-Uribe, B. Esteban-Fernández de Ávila, N. Krishnan, C. Xiao, C.J. Ventura, H. Gong, Q. Zhang, W. Gao, Physical disruption of solid tumors by immunostimulatory microrobots enhances antitumor immunity, Adv. Mater. 33 (49) (2021) 2103505.

[48] C.E. Witherel, K. Sao, B.K. Brisson, B. Han, S.W. Volk, R.J. Petrie, L. Han, K. L. Spiller, Regulation of extracellular matrix assembly and structure by hybrid M1/M2 macrophages, Biomaterials 269 (2021) 120667.

[49] L. Chen, Z. Yao, S. Zhang, K. Tang, Q. Yang, Y. Wang, B. Li, Y. Nie, X. Tian, L. Sun, Biomaterial-induced macrophage polarization for bone regeneration, Chin. Chem. Lett. 34 (6) (2023) 107925.

[50] W. Qiao, K.H. Wong, J. Shen, W. Wang, J. Wu, J. Li, Z. Lin, Z. Chen, J. P. Matinlinna, Y. Zheng, TRPM7 kinase-mediated immunomodulation in macrophage plays a central role in magnesium ion-induced bone regeneration, Nat. Commun. 12 (1) (2021) 2885.

[51] C. Gao, W. Dai, X. Wang, L. Zhang, Y. Wang, Y. Huang, Z. Yuan, X. Zhang, Y. Yu, X. Yang, Magnesium gradient-based hierarchical scaffold for dual-lineage regeneration of osteochondral defect, Adv. Funct. Mater. 33 (43) (2023) 2304829.

[52] L. Zheng, S. Zhao, Y. Li, J. Xu, W. Yan, B. Guo, J. Xu, L. Jiang, Y. Zhang, H. Wei, Engineered MgO nanoparticles for cartilage-bone synergistic therapy, Sci. Adv. 10 (10) (2024) eadk6084.